LETTER

https://doi.org/10.1038/s41586-019-1139-x

A late Middle Pleistocene Denisovan mandible from the Tibetan Plateau

Fahu Chen[1,2,15]*, Frido Welker[2,3,4,15], Chuan-Chou Shen[5,6,15], Shara E. Bailey[3,7], Inga Bergmann[3], Simon Davis[8], Huan Xia[2], Hui Wang[9,10], Roman Fischer[8], Sarah E. Freidline[3], Tsai-Luen Yu[5,6], Matthew M. Skinner[3,11], Stefanie Stelzer[3,12], Guangrong Dong[2], Qiaomei Fu[13], Guanghui Dong[2], Jian Wang[2], Dongju Zhang[2]* & Jean-Jacques Hublin[3,14]*

Denisovans are members of a hominin group who are currently only known directly from fragmentary fossils, the genomes of which have been studied from a single site, Denisova Cave[1–3] in Siberia. They are also known indirectly from their genetic legacy through gene flow into several low-altitude East Asian populations[4,5] and high-altitude modern Tibetans[6]. The lack of morphologically informative Denisovan fossils hinders our ability to connect geographically and temporally dispersed fossil hominins from Asia and to understand in a coherent manner their relation to recent Asian populations. This includes understanding the genetic adaptation of humans to the high-altitude Tibetan Plateau[7,8], which was inherited from the Denisovans. Here we report a Denisovan mandible, identified by ancient protein analysis[9,10], found on the Tibetan Plateau in Baishiya Karst Cave, Xiahe, Gansu, China. We determine the mandible to be at least 160 thousand years old through U-series dating of an adhering carbonate matrix. The Xiahe specimen provides direct evidence of the Denisovans outside the Altai Mountains and its analysis unique insights into Denisovan mandibular and dental morphology. Our results indicate that archaic hominins occupied the Tibetan Plateau in the Middle Pleistocene epoch and successfully adapted to high-altitude hypoxic environments long before the regional arrival of modern *Homo sapiens*.

Denisovans are an extinct sister group of Neanderthals and are only known from fragmentary fossils that have been identified at Denisova Cave (Altai, Russia; Extended Data Fig. 1a). Their genomic legacy is present in several Asian, Australian and Melanesian populations[4,11–14], suggesting that they once might have been widespread. Denisovan introgression into present day Tibetans, Sherpas and neighbouring populations includes positive selection for the Denisovan allele of the endothelial PAS domain-containing protein 1 (*EPAS1*), which provides high-altitude adaptation to hypoxia in extant humans who inhabit the Tibetan Plateau[6,15,16]. This Denisovan-derived adaptation is currently difficult to reconcile with the low altitude of Denisova Cave (700 m altitude) and the earliest evidence of a high-altitude presence of humans on the Tibetan Plateau around 30–40 thousand years before present (kyr BP; taken as AD 1950)[17–20]. Furthermore, the relationships of various Middle Pleistocene and Late Pleistocene hominin fossils in East Asia with Denisovans are difficult to resolve owing to limited morphological information on Denisovans and the lack of palaeogenetic data on Middle Pleistocene hominin fossils from East Asia and tropical Oceania.

The right half of a hominin mandible (hereafter Xiahe mandible) was found in Baishiya Karst Cave in 1980 (3,280 m altitude; Fig. 1 and Extended Data Figs. 2, 3). A recent excavation revealed the presence of abundant Palaeolithic stone artefacts and cut-marked animal bones in Baishiya Karst Cave (Extended Data Fig. 1b). An in situ carbonate matrix is present on the bottom of the specimen, enabling determination of a minimum age for the Xiahe mandible. Three carbonate subsamples were collected for U–Th dating (see Methods and Supplementary Information). The bulk ^{230}Th age of 164.5 ± 6.2 kyr BP is not statistically different from the age of 155 ± 15 kyr BP that was obtained for the uppermost and 163 ± 10 kyr BP for the lowermost parts of the crust (Student's *t*-test, $P < 0.05$; Extended Data Table 1 and Supplementary Information). Consistency between the ages of the subsamples from different places of the carbonate indicates that this crust formed in a short time period around 160 kyr BP. Hominins therefore occupied the Tibetan Plateau at least as early as marine isotope stage 6 in the penultimate glacial period.

There is no evidence for the preservation of ancient DNA in the Xiahe mandible (Methods). However, palaeoproteomic analysis revealed the survival of an endogenous ancient proteome in a dentine sample, but not in a bone sample[9,21] (Extended Data Fig. 4 and Methods). The endogenous proteins are highly degraded and clearly distinguishable from contaminating modern proteins (Extended Data Table 2 and Extended Data Figs. 4, 5). Phylogenetic analysis of the recovered proteome results in a phylogenetic tree that accurately reflects the phylogeny of the great apes, including the relationships between *H. sapiens*, Neanderthals and Denisovans (Fig. 2). Within this framework, the Xiahe proteome is placed together with the Denisovan high-coverage genome[22] (Denisova Cave individual D3; Bayesian probability = 0.99). In addition, the observed state of particular single amino acid polymorphisms within the Xiahe proteome further supports the close relationship between the Xiahe proteome and Denisovans (Supplementary Information). Only one high-coverage Denisovan genome is currently available (D3), limiting our understanding of the proteomic sequence diversity within Denisovans. We therefore assign the Xiahe mandible to a hominin population closely related to the Denisovans from Denisova Cave.

The Xiahe mandible is heavily encrusted in a carbonate matrix (Extended Data Fig. 2). The carbonate matrix is the only in situ material that can be directly associated with the mandible. We therefore scanned the specimen using micro-computed tomography and removed the carbonate matrix virtually by manual segmentation (see Methods). The Xiahe mandible displays an archaic morphology that is rather common among Middle Pleistocene hominins. Metrically, the fossil is within the variation of this group (Supplementary Table 2 and

[1]Key Laboratory of Alpine Ecology (LAE), CAS Center for Excellence in Tibetan Plateau Earth Sciences and Institute of Tibetan Plateau Research, Chinese Academy of Sciences, Beijing, China. [2]Key Laboratory of Western China's Environmental Systems (Ministry of Education), College of Earth and Environmental Sciences, Lanzhou University, Lanzhou, China. [3]Department of Human Evolution, Max Planck Institute for Evolutionary Anthropology, Leipzig, Germany. [4]Department of Biology, University of Copenhagen, Copenhagen, Denmark. [5]High-Precision Mass Spectrometry and Environment Change Laboratory (HISPEC), Department of Geosciences, National Taiwan University, Taipei, Taiwan, China. [6]Research Center for Future Earth, National Taiwan University, Taipei, Taiwan, China. [7]Department of Anthropology, Center for the Study of Human Origins, New York University, New York, NY, USA. [8]Target Discovery Institute, University of Oxford, Oxford, UK. [9]Department of Cultural Heritage and Museology, Institute of Archaeological Science, Fudan University, Shanghai, China. [10]Gansu Provincial Institute of Cultural Relics and Archaeological Research, Lanzhou, China. [11]School of Anthropology and Conservation, University of Kent, Canterbury, UK. [12]Department of Anatomy and Biomechanics, Karl Landsteiner University of Health Sciences, Krems an der Donau, Austria. [13]Key Laboratory of Vertebrate Evolution and Human Origins, Center for Excellence in Life and Paleoenvironment, Institute of Vertebrate Paleontology and Paleoanthropology, Chinese Academy of Sciences, Beijing, China. [14]Chaire Internationale de Paléoanthropologie, Collège de France, Paris, France. [15]These authors contributed equally: Fahu Chen, Frido Welker, Chuan-Chou Shen. *e-mail: fhchen@itpcas.ac.cn; djzhang@lzu.edu.cn; hublin@eva.mpg.de

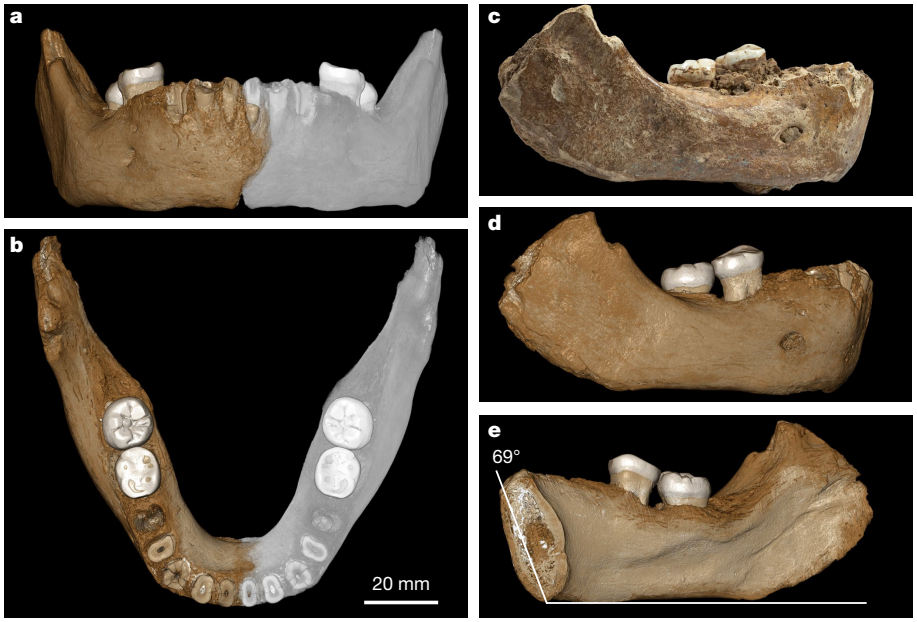

Fig. 1 | The Xiahe mandible. a–**e**, Anterior (**a**), occlusal (**b**), lateral (**c**, **d**) and internal (**e**) views of the specimen. **a**, **b**, **d**, **e**, Views after digital removal of the adhering carbonate matrix. The preservation of the symphyseal region of the mandible allows for a virtual reconstruction of the two sides of the mandible. Mirrored parts are in grey. The symphyseal section and the infradentale–gnathion angle are displayed in **e**.

Supplementary Fig. 2). The body is very robust, relatively low and thick. Its height slightly decreases towards the back. There is a pronounced lateral prominence and a well-developed anterior marginal tubercle. Internally, a protruding alveolar prominence overhangs a marked sub-alveolar fossa. From the mandibular foramen, the mylohyoid line runs in a low position. The mental foramen is located under the P_4 and low on the body. Although a triangular mental protuberance is weakly expressed, there is no developed chin and the symphysis is strongly receding with an inclination angle of 69° (Fig. 1e). Lingually, a primitive pattern of a small genioglossal fossa that separates the upper and lower transverse tori is present. The primitive morphology of the Xiahe mandible is confirmed by geometric morphometric analysis, where it falls within the sample of Middle Pleistocene specimens and at the limit of the *Homo erectus* distribution, close to the Chinese Lantian and Zhoukoudian GI/II and H1.12 specimens (Extended Data Fig. 6). By contrast, it is well-separated from *H. erectus* in the geometric morphometric analysis of dental arcade shape (Extended Data Fig. 7); it is less elongated than *H. erectus* and plots close to primitive specimens of Middle Pleistocene hominins, Neanderthals and *H. sapiens*.

The dental morphology also fits within Middle Pleistocene hominin variability. The M_1 has five well-developed primary cusps and a Y-fissure pattern. In addition, it has two accessory cusps: tuberculum sextum (C6) and tuberculum intermedium (C7; Supplementary Table 4). The middle-trigonid crest is absent from the outer enamel surface, but is present at the enamel–dentine junction (EDJ) as a low continuous crest that dips at the sagittal sulcus (grade 2 in a previously published study[23]; Extended Data Fig. 8). There are two wide roots—mesial and distal—each with bifurcated apices. The M_2, which was erupting but already in functional occlusion, preserves the five principal cusps arranged in a Y-pattern and a large C7 (Supplementary Table 4). The between-group principal component analysis of the EDJ ridge and cervix shape groups the Xiahe M_2 with other Middle Pleistocene specimens, such as Mauer and Balanica, but away from the distribution of *H. erectus* specimens (Extended Data Fig. 8b).

The assignment of the Xiahe mandible to the Denisovans or a closely related sister population orients the morphological comparisons towards the Denisovan specimens from Denisova Cave, their sister group the Neanderthals and penecontemporaneous East Asian specimens. Xiahe lacks the high mandibular body that is observed in specimens from Neanderthals and its symphyseal profile is more receding; however, the shape of the anteriorly broad and flattened dental arcade is reminiscent of Neanderthals (Supplementary Figs. 2, 3). There is also a marked retromolar space that is commonly observed in Neanderthals, although this feature might be linked to the agenesis of the M_3.

The feature of the Xiahe specimen that best links it to the fragmentary fossils from Denisova Cave is its large dentition. In geometric morphometric form space, the size of the Xiahe dental arcade is close to that of Tighénif 3 and Irhoud 11 and surpasses all the other comparative specimens along between-group principal component 1, with the exception of KNM-WT15000 (Extended Data Fig. 7). The combination of a moderately large mandible with an exceptionally large dental arcade is confirmed by analysis of the teeth. The bucco-lingual diameter of the M_1 is larger than the mean of all Middle Pleistocene samples and exceeds the maximum value of the Middle Pleistocene European samples (Supplementary Table 3). Its mesio-distal diameter is larger than, and outside the range of, all of our comparative specimens. The M_2 has a bucco-lingual diameter at the high end of the range of *H. erectus* specimens. Its mesio-distal diameter is within the range of the Middle Pleistocene European sample but outside the range of the rest of the comparative samples (Supplementary Table 3).

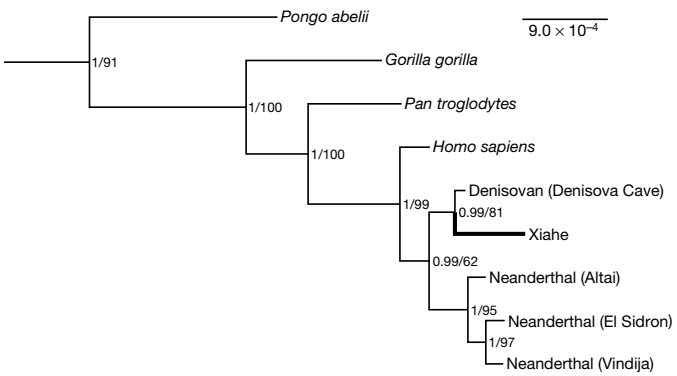

Fig. 2 | Phylogenetic position of the Xiahe proteome within Hominidae. Node values indicate Bayesian probability (0–1)/RAxML maximum likelihood (0–100%), respectively. *Macaca macaca* and *Nomascus leucogenys* are used as outgroups (data not shown).

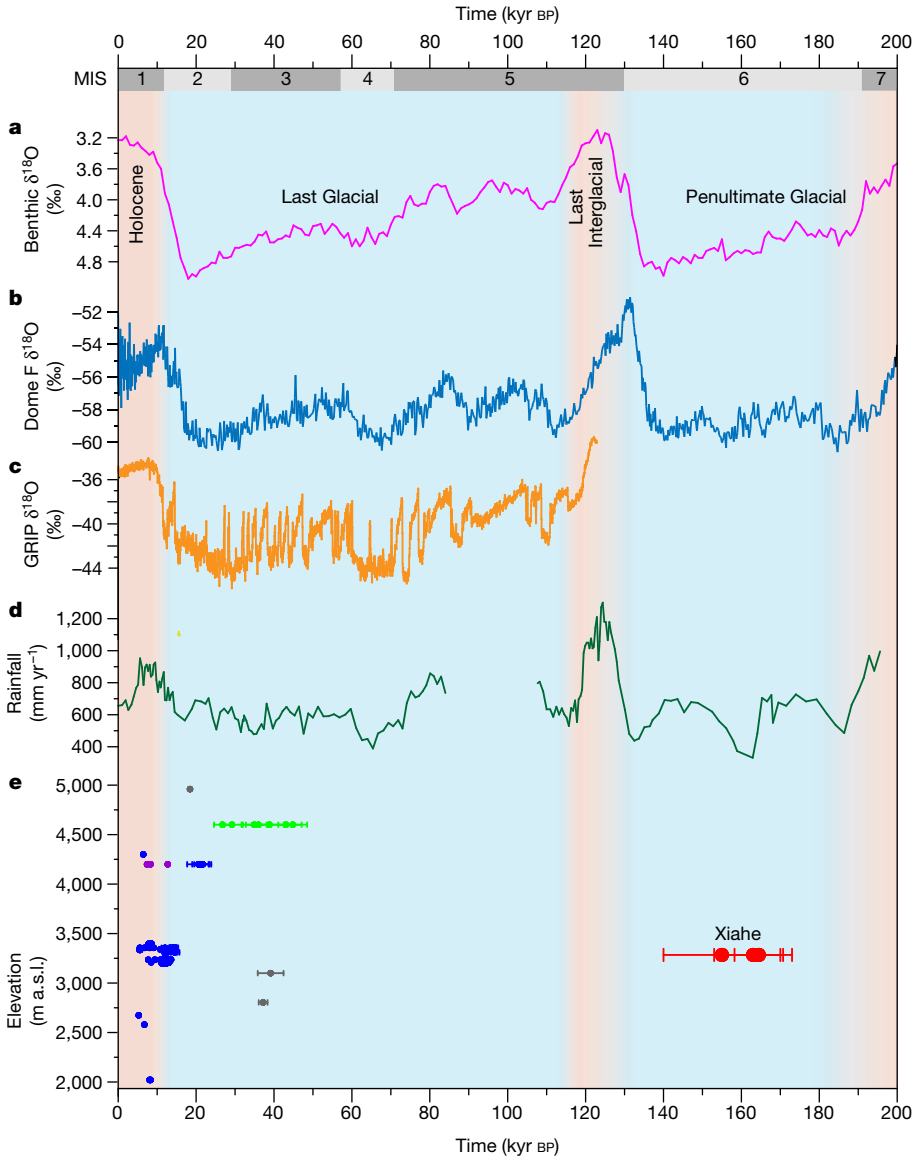

Fig. 3 | The palaeoclimate background to human presence on the Tibetan Plateau. a, LR04 benthic stack $\delta^{18}O$ records[28]. **b**, Antarctic Fuji Dome F ice core $\delta^{18}O$ isotope data[29]. **c**, Greenland Ice Sheet Project (GRIP) $\delta^{18}O$ isotope data[30]. **d**, The ^{10}Be-based rainfall for Loess samples from Baoji, China[31]. **e**, Available absolute dates of Palaeolithic and Epi-Palaeolithic sites on the Tibetan Plateau (see Methods). masl, metres above sea level; MIS, marine isotope stage.

Among the penecontemporaneous East Asian specimens, Xiahe is comparable to the Penghu 1 mandible[24] in several aspects. A three-dimensional surface model of Penghu 1 is not available for geometric morphometric analysis but the bone metrics (Supplementary Table 2) and dental morphology are very similar. Like Xiahe, Penghu 1 displays agenesis of the M_3. Although the M_2 of Penghu 1 is smaller than that of Xiahe, in both individuals the M_2 crown is wider mesio-distally than bucco-lingualy. The M_2 roots of the Xiahe and Penghu 1 specimens are remarkable. In addition to mesial and distal plate-like roots, there is a prominent accessory lingual root that branches off the mesial root below the cervix. This feature is of particular interest as three-rooted mandibular molars are very rare in non-Asian *H. sapiens* but appear much more frequently in recent Asian populations (see Supplementary Information). Finally, in both specimens, the P_3 displays Tomes' root, a feature occasionally observed in other fossil hominins (Extended Data Fig. 8a). Among other non-*H. sapiens* Chinese specimens, the EDJ of both Xiahe and Xujiayao molars exhibit moderately complex occlusal basins, and the Xiahe M_2 and Xujiayao M_3 possess a similar protostylid crest[25]. Notably, similar to the Xiahe mandible, morphological similarities to Neanderthals have also been described for cranial remains from Xujiayao and Xuchang. These observations reinforce the idea that Denisovans are already represented in the fossil record of China, particularly in fossils such as Penghu 1 and Xujiayao. Future ancient DNA and ancient protein analysis of these specimens can directly test this hypothesis.

The Xiahe mandible is, to our knowledge, the first Denisovan identified outside of Denisova Cave[1,11]. The minimum age of the mandible (of approximately 160 kyr BP) makes the Xiahe mandible comparable in age to Denisova 2, chronologically the oldest Denisovan fossil that is currently known from Denisova Cave[2,3,26]. Neanderthals and Denisovans are estimated to have diverged around 445–473 thousand years ago[27]. The early part of the Denisovan lineage, therefore, remains undocumented in the fossil record. However, the Xiahe mandible demonstrates that Denisovans or Denisovan-related populations have deep roots in central East Asia.

The Xiahe mandible represents, as far as we know, the earliest hominin fossil on the Tibetan Plateau. It is at least 120 thousand years older than the oldest known Palaeolithic sites (30–40 kyr BP) in the region[17,20] (Fig. 3). Successful colonization of, and adaptation to, high-altitude plateaus such as the Himalayas has generally been considered to be

restricted to recent *H. sapiens*[20], particularly because of adverse conditions, such as resource scarcity, low temperatures and hypoxia. Instead, the Xiahe mandible demonstrates that archaic hominins occupied the Tibetan Plateau and successfully adapted to such environments (Fig. 3). The evidence suggests that Denisovans or Denisovan-related populations accumulated adaptive alleles that are beneficial to the occupation of high-altitude environments during their presence on the Tibetan Plateau. Archaic hominin alleles in modern Himalayan populations, such as the Denisovan-derived *EPAS1* allele[6,16], may therefore derive from a local archaic hominin on or around the Tibetan Plateau, such as the Xiahe hominin population.

The Xiahe Denisovan provides evidence of a deep evolutionary history of these archaic hominins within the challenging environment of the Tibetan Plateau. Its mandibular and dental anatomy relates other Chinese fossil hominins to the Denisovans and its discovery resolves several outstanding questions concerning this important hominin group. Our analyses pave the way towards a better understanding of the evolutionary history of Middle Pleistocene hominins in East Asia.

Online content

Any methods, additional references, Nature Research reporting summaries, source data, statements of data availability and associated accession codes are available at https://doi.org/10.1038/s41586-019-1139-x.

Received: 10 December 2018; Accepted: 25 March 2019;

1. Krause, J. et al. The complete mitochondrial DNA genome of an unknown hominin from southern Siberia. *Nature* **464**, 894–897 (2010).
2. Sawyer, S. et al. Nuclear and mitochondrial DNA sequences from two Denisovan individuals. *Proc. Natl Acad. Sci. USA* **112**, 15696–15700 (2015).
3. Slon, V. et al. A fourth Denisovan individual. *Sci. Adv.* **3**, e1700186 (2017).
4. Browning, S. R., Browning, B. L., Zhou, Y., Tucci, S. & Akey, J. M. Analysis of human sequence data reveals two pulses of archaic Denisovan admixture. *Cell* **173**, 53–61 (2018).
5. Sankararaman, S., Mallick, S., Patterson, N. & Reich, D. The combined landscape of Denisovan and Neanderthal ancestry in present-day humans. *Curr. Biol.* **26**, 1241–1247 (2016).
6. Huerta-Sánchez, E. et al. Altitude adaptation in Tibetans caused by introgression of Denisovan-like DNA. *Nature* **512**, 194–197 (2014).
7. Chen, F. H. et al. Agriculture facilitated permanent human occupation of the Tibetan Plateau after 3600 B.P. *Science* **347**, 248–250 (2015).
8. Meyer, M. C. et al. Permanent human occupation of the central Tibetan Plateau in the early Holocene. *Science* **355**, 64–67 (2017).
9. Welker, F. Palaeoproteomics for human evolution studies. *Quat. Sci. Rev.* **190**, 137–147 (2018).
10. Welker, F. Elucidation of cross-species proteomic effects in human and hominin bone proteome identification through a bioinformatics experiment. *BMC Evol. Biol.* **18**, 23 (2018).
11. Reich, D. et al. Genetic history of an archaic hominin group from Denisova Cave in Siberia. *Nature* **468**, 1053–1060 (2010).
12. Qin, P. & Stoneking, M. Denisovan ancestry in East Eurasian and Native American populations. *Mol. Biol. Evol.* **32**, 2665–2674 (2015).
13. Skoglund, P. & Jakobsson, M. Archaic human ancestry in East Asia. *Proc. Natl Acad. Sci. USA* **108**, 18301–18306 (2011).
14. Reich, D. et al. Denisova admixture and the first modern human dispersals into Southeast Asia and Oceania. *Am. J. Hum. Genet.* **89**, 516–528 (2011).
15. Jeong, C. et al. Admixture facilitates genetic adaptations to high altitude in Tibet. *Nat. Commun.* **5**, 3281 (2014).
16. Hackinger, S. et al. Wide distribution and altitude correlation of an archaic high-altitude-adaptive *EPAS1* haplotype in the Himalayas. *Hum. Genet.* **135**, 393–402 (2016).
17. Zhang, D. et al. History and possible mechanisms of prehistoric human migration to the Tibetan Plateau. *Sci. China Earth Sci.* **59**, 1765–1778 (2016).
18. Yuan, B., Huang, W. & Zhang, D. New evidence for human occupation of the northern Tibetan Plateau, China during the Late Pleistocene. *Chin. Sci. Bull.* **52**, 2675–2679 (2007).
19. Zhao, M. et al. Mitochondrial genome evidence reveals successful Late Paleolithic settlement on the Tibetan Plateau. *Proc. Natl Acad. Sci. USA* **106**, 21230–21235 (2009).
20. Zhang, X. L. et al. The earliest human occupation of the high-altitude Tibetan Plateau 40 thousand to 30 thousand years ago. *Science* **362**, 1049–1051 (2018).
21. Welker, F. et al. Palaeoproteomic evidence identifies archaic hominins associated with the Châtelperronian at the Grotte du Renne. *Proc. Natl Acad. Sci. USA* **113**, 11162–11167 (2016).
22. Meyer, M. et al. A high-coverage genome sequence from an archaic Denisovan individual. *Science* **338**, 222–226 (2012).
23. Bailey, S. E., Skinner, M. M. & Hublin, J.-J. What lies beneath? An evaluation of lower molar trigonid crest patterns based on both dentine and enamel expression. *Am. J. Phys. Anthropol.* **145**, 505–518 (2011).
24. Chang, C.-H. et al. The first archaic *Homo* from Taiwan. *Nat. Commun.* **6**, 6037 (2015).
25. Xing, S., Martinón-Torres, M., Bermúdez de Castro, J. M., Wu, X. & Liu, W. Hominin teeth from the early Late Pleistocene site of Xujiayao, Northern China. *Am. J. Phys. Anthropol.* **156**, 224–240 (2015).
26. Douka, K. et al. Age estimates for hominin fossils and the onset of the Upper Palaeolithic at Denisova Cave. *Nature* **565**, 640–644 (2019).
27. Prüfer, K. et al. The complete genome sequence of a Neanderthal from the Altai Mountains. *Nature* **505**, 43–49 (2014).
28. Lisiecki, L. E. & Raymo, M. E. A Pliocene–Pleistocene stack of 57 globally distributed benthic $\delta^{18}O$ records. *Paleoceanography* **20**, PA1003 (2005).
29. Uemura, R. et al. Ranges of moisture-source temperature estimated from Antarctic ice cores stable isotope records over glacial–interglacial cycles. *Clim. Past* **8**, 1109–1125 (2012).
30. North Greenland Ice Core Project members. High-resolution record of Northern Hemisphere climate extending into the last interglacial period. *Nature* **431**, 147–151 (2004).
31. Beck, J. W. et al. A 550,000-year record of East Asian monsoon rainfall from ^{10}Be in loess. *Science* **360**, 877–881 (2018).

Acknowledgements We thank the sixth Gung-Thang Living Buddha, the anonymous monk, L. L. Wang and her husband for providing us the opportunity to study the fossil; D. Madsen, J. Brantingham, D. Rhode, C. Perreault, J. S. Yang, T. Cheng, X. K. Shen, J. T. Yao, Z. X. Yang, J. Chen, X. Z. Huang, M. H. Qiu and C.-R. Huang for their assistance with the fieldwork and in the laboratory; members of the local government of Xiahe County and Ganjia town for help, the monks in the Baishiya temple and people from Bajiao Ancient City for their support of the fieldwork; O. Jöris, G. Smith, P. Ungar, R. Grün for discussions and comments; many curators and colleagues who, over the years, gave us access to recent and fossil hominin specimens for computed tomography scanning, photogrammetry or analysis; E. Trinkaus for providing comparative data; H. Temming, S. Tuepke, C. Molenaar and Diondo for their technical assistance; S. Pääbo, V. Slon and A. Ayinuer-Petri for ancient DNA analytical support. We received support from the Strategic Priority Research Program of Chinese Academy of Sciences, Pan-Third Pole Environment Study for a Green Silk Road (Pan-TPE) (XDA20040000) and National Natural Science Foundation of China (41620104007). D.J.Z. received support from National Natural Science Foundation of China (41771225). Fieldwork in 2018 was supported by the Second Tibetan Plateau Scientific Expedition (Project no. 4). U–Th dating was supported by the Science Vanguard Research Program of the Ministry of Science and Technology (107-2119-M-002-051) and the Higher Education Sprout Project of the Ministry of Education, Taiwan (107L901001). J.-J.H. and F.W. thank the Max Planck Society for providing financial support.

Reviewer information *Nature* thanks Aida Gómez-Robles, Antonio Rosas and the other anonymous reviewer(s) for their contribution to the peer review of this work.

Author contributions F.H.C., J.-J.H. and D.J.Z. designed the study. D.J.Z., G.R.D., G.H.D., H.W., J.W. and H.X. collected field data. D.J.Z., H.X. and J.W. carried out sampling and subsampling process. C.-C.S. and T.-L.Y. conducted U–Th dating of the crust carbonates. Q.M.F. performed the ancient DNA extractions. Mandibular metrical and non-metrical data were compiled and analysed by J.-J.H. and I.B. Geometric morphometric analyses of the mandible were performed by S.E.F., S.S., I.B., D.J.Z. and J.-J.H. Dental metrical and non-metrical data were compiled and analysed by S.E.B. and M.M.S. H.X., F.W., R.F. and S.D. performed proteomic analysis. F.H.C., F.W., J.-J.H., D.J.Z. and C.-C.S. wrote the paper with contributions of all authors.

Competing interests The authors declare no competing interests.

Additional information

Extended data is available for this paper at https://doi.org/10.1038/s41586-019-1139-x.
Supplementary information is available for this paper at https://doi.org/10.1038/s41586-019-1139-x.
Reprints and permissions information is available at http://www.nature.com/reprints.
Correspondence and requests for materials should be addressed to F.C., D.Z. or J.-J.H.
Publisher's note: Springer Nature remains neutral with regard to jurisdictional claims in published maps and institutional affiliations.

METHODS

Study site. Baishiya Karst Cave, which is 3,280 m above sea level, is located on the south face of the Dalijiashan mountain in Ganjia Basin, Xiahe county, Gansu province, China, on the northeastern Tibetan Plateau (Extended Data Fig. 1). The cave is located at the mouth of the Jiangla river, a small tributary of the Yangqu river in the Ganjia Basin. This cave, with a 10-m high and 20-m wide entrance and several chambers, is more than 1 km long. The studied fossil mandible was found in 1980. Extensive surveys and test excavations in the cave and surrounding regions have been conducted since 2011. Various animal bones with cut marks and stone artefacts, including flakes, cores and scrapers were discovered in the thick deposits of the cave entrance. Two nearby Palaeolithic sites discovered in 2016 suggest that prehistoric human activity was not restricted to the cave but was also present in the open-air regions of Ganjia Basin (Extended Data Fig. 1b).

Chronological dates for archaeological sites on the Tibetan Plateau (Fig. 3e) were taken from the following literature. Dates in blue (from various sites) were previously described[7,32]. Dates in purple (the Quesang site) were published previously[8]. Dates in green (the Nwya Devu site) were previously published[20]. Grey symbols (Wulunwula lake site, Siling Co and Lenghu sites) represent indirect or disputed dates published elsewhere[33]. Dates in red are those reported here for the Xiahe mandible. This overview clearly demonstrates that the Xiahe hominin is a minimum of 120 kyr older than any previously identified hominin occupation of the Tibetan Plateau.

U–Th dating. U–Th dating was performed on one bulk sample and two serial samples of carbonate crust adhering to the Xiahe mandible (Supplementary Fig. 1). After an ultrasonic cleaning step with ultrapure water, U–Th dating was applied to the three subsamples. Procedures were conducted in a class-10,000 clean room with class-100 benches at the High-Precision Mass Spectrometry and Environment Change Laboratory[34]. Each subsample was dissolved in nitric acid, spiked with a ^{233}U–^{236}U–^{229}Th tracer, and then refluxed at 90–100 °C overnight. Uranium and thorium were purified with chemical methods including Fe co-precipitation and anion-exchange chromatography[35]. Isotopic compositions were determined on a Thermo-Finnigan NEPTUNE multi-collector inductively coupled plasma mass spectrometer[35]. U–Th uncertainties were calculated to the 2σ level. U–Th isotopic compositions, activities and ^{230}Th dates—in years before AD 1950—with 2σ error are given in Extended Data Table 1. Further details on U–Th can be found in the Supplementary Information.

Morphological analyses. A list of all specimens used in various morphological comparisons with extant and other fossil hominins can be found in Supplementary Table 6.

Computed tomography and virtual reconstruction of the fossil. The original fossil specimen was scanned using a Diondo d3 industrial micro-computed tomography scanner (Diodon) at the DCS Engineering Innovation Laboratory. The specimen was scanned with an isotropic voxel size of 52.125 μm. Segmentation of the micro-computed tomography volume was performed in Avizo (Visualization Sciences Group). The comparative dental sample was scanned with an isotropic voxel size ranging from 11.6 to 39.1 μm at the MPI-EVA on a BIR ARCTIS 225/300 micro-computed tomography scanner or on a Skyscan 1172 micro-computed tomography scanner. The micro-computed tomography slices were filtered using a median filter followed by a mean-of-least-variance filter to reduce the background noise while preserving and enhancing edges. The matrix adhering to the mandible was virtually removed by manual segmentation. The specimen was reconstructed with Aviso by mirroring the right side of the mandible to the left in the position that allowed the best anatomical match of the overlapping symphyseal regions.

Mandibular metric data. Three-dimensional surface models of recent *H. sapiens* (Department of Life Sciences, University of Coimbra) and fossil mandibles were obtained from computed tomography scans, NextEngine laser scans or photogrammetric methods (Supplementary Table 6). For the photogrammetric methods, between 40 and 90 photographs were taken of each mandible with a Nikon camera. After excluding the background of each image, the photographs were processed by Agisoft PhotoScan software. Each stack of photographs ran through alignment, geometric reconstruction and texturing steps in order to return a three-dimensional surface model. This method has been proven equivalent in accuracy and precision to conventional imaging techniques (see Supplementary Information). For most fossils, surface models were made from the original specimen; however, in several instances research-quality casts were used. Linear measurements were taken on three-dimensional surface models. Data generated through these various methods are comparable in terms of quality and precision (Supplementary Table 1). Our measurements were complemented by measurements of the original specimens taken by E. Trinkaus (height and breadth of the mandibular corpus at the level of the mental foramen) and comparative data taken from the literature (see Supplementary Table 6).

Shape analysis of the mandible. Geometric morphometric methods were used to analyse the shape of the Xiahe mandible in a comparative context. Three-dimensional coordinates of anatomical landmarks and curve semilandmarks ($n = 88$) were digitized on the surface models ($n = 170$) using Landmark Editor[36] according to the preserved morphology of the Xiahe mandible. Landmark and semilandmark data were analysed in R. Missing bilateral landmarks and curve semilandmarks were estimated by mirroring the preserved side. Missing landmarks and curve semilandmarks that lacked a bilateral counterpart were estimated by deforming the sample average onto the deficient configuration using thin-plate spline interpolation. Curve semilandmarks were slid by minimizing the bending energy of a thin-plate spline deformation between each specimen and the sample mean shape[37]. After sliding, all landmarks and curve semilandmarks were converted to shape variables using a generalized Procrustes analysis. The resulting shape coordinates were analysed using a between-group principal component analysis (bgPCA)[38]. To do so, the sample was divided into six a priori groups (*H. erectus*, Middle Pleistocene hominins, Neanderthals, early *H. sapiens*, Upper Palaeolithic *H. sapiens* and recent *H. sapiens*). The covariance matrix of the a priori group means was calculated and projected into the eigenspace of the first two eigenvectors (bgPC1 and bgPC2). Xiahe was not included in the calculation and subsequently projected into the eigenspace. Shape changes were visualized along bgPC1 and bgPC2 by warping the sample mean shape along the positive and negative ends of bgPC1 and bgPC2, $\pm 2\sigma$ from the sample mean.

Shape analysis of the dental arcade. Geometric morphometric methods were used to analyse the shape of the dental arcade of the Xiahe mandible. Three-dimensional landmark data were collected on computed tomographic scans and surface scans of recent *H. sapiens* ($n = 52$) and fossil ($n = 42$) specimens. Specimens of recent *H. sapiens* were scanned using industrial micro-computed tomography (BIR ACTIS 225/300 at the MPI-EVA; isotropic voxel sizes of 0.03–0.093 mm), and medical computed tomography (Vivantes Klinikum Berlin, CIMED and the Smithsonian National Museum of Natural History, Washington DC[39]); pixel sizes of 0.13–0.47 mm, slice intervals of 0.33–0.50 mm). The fossil hominin samples comprise computed tomography and surface scans of the original fossils and casts, which were obtained at the MPI-EVA. To capture mandibular arcade shape, spatial arrangement of the teeth and dental size proportions, landmarks were taken on the alveolar margin of every tooth except the third molars. Additionally, landmarks were taken at the cervix of the first and second molars because these teeth are preserved in Xiahe. The landmarks were placed at the most distal, buccal, mesial and lingual tooth dimensions on the alveolar bone of the incisors, canines and premolars. For the molars, a mesial and a distal landmark, as well as two landmarks were taken at the most exposed position of the mesial and distal root. The cervical landmarks on M_1 and M_2 were placed at the most distal, buccal, mesial and lingual position. Missing data were estimated by thin-plate spline warping. All measurements were taken in Avizo. Landmarks were symmetrized using reflected relabelling[40] and superimposed by applying the generalized Procrustes analysis[41,42]. To create a larger comparative sample set, we estimated mandibular arcades from maxillary arcades following the protocol described previously[43–45]. Therefore, the same landmarks protocol as described above was applied to the maxillary arcades of fossils that lack lower jaws. To estimate mandibular arcades for these individuals, we used multiple multivariate regression based on the covariation between maxillary and mandibular landmarks. To analyse differences in shape, we performed a bgPCA on the Procrustes shape coordinates. To analyse the impact of size, we added the variable log centroid size to the Procrustes shape variables and computed a bgPCA in form space. The inclusion of estimated dental arcade wireframes based on available maxillary arcades (Extended Data Fig. 7) results in the same relationship of Xiahe to other hominin fossils in both shape and form space as when such estimated mandibular arcades are excluded from the analysis (Supplementary Fig. 3). All statistical analyses were performed in Mathematica[46].

Dental metric and non-metric data. Crown metric and non-metric data were collected from casts or originals, with a few exceptions, which were taken from the literature (see Supplementary Information for details on exceptions). Root metric data were taken on three-dimensional models generated from micro-computed tomographic data. Crown measurements were taken using Mitutuyo digital callipers. Non-metric trait expressions were scored using the Arizona State University Dental Anthropology System[47] where applicable (for lower dentition: cusp 6, cusp 7, molar groove pattern and protostylid) and using a previously published protocol[23] for the middle trigonid crest. The recent *H. sapiens* sample includes individuals from southern, western and eastern Africa, western and central Europe, northeastern Asia, western Asia, India, Australia, New Guinea and Andaman Islands.

Molar EDJ shape analysis. Enamel and dentine tissues (Extended Data Fig. 8) of lower second molars were segmented using the three-dimensional voxel value histogram and its distribution of greyscale values[48,49]. After segmentation, the EDJ was reconstructed as a triangle-based surface model using Avizo. Small EDJ defects were corrected digitally using the 'fill holes' module of Geomagic Studio. We then used Avizo to digitize three-dimensional landmarks and curve-semilandmarks on these EDJ surfaces[48,49]. Anatomical landmarks were placed on the tip of the dentine horn of the protoconid, metaconid, entoconid and hypoconid. A sequence

of landmarks was also placed along the marginal ridge that connected the dentine horns beginning at the top of the protoconid moving in lingual direction; the points along this ridge curve were then later resampled to the same point count on every specimen using Mathematica. Similarly, we digitized and resampled a curve along the cemento–enamel junction as a closed curve starting and ending below the protoconid horn and the mesiobuccal corner of the cervix. The resampled points along the two ridge curves were subsequently treated as sliding curve semilandmarks and analysed using geometric morphometric together with the four anatomical landmarks.

Ancient DNA analysis. We prepared one extract from 64.3 mg of dentine powder from the Xiahe mandible[50]. From this extract (10 μl out of 50 μl), we produced one library using a single-stranded library protocol[22,51]. We captured the human mitochondrial DNA (mtDNA) genome sequences from this library using an in-solution capture method[52] to determine the DNA preservation. We sequenced the enriched library on a MiSeq using a double index configuration (2 × 76 bp) and merged the forward and reverse sequences into a single fragment requiring an overlap of at least 11 bp. We mapped these merged reads, which we call a 'fragment', to the revised Cambridge reference sequence (rCRS NC_012920) using bwa[53] with the following parameters: –n 0.01 and –l 16500. We removed duplicate fragments by identifying all fragments with the same start and end positions and keeping the one with the highest average base quality.

We observe no ancient damage pattern, which suggests that the Xiahe mandible does not contain ancient human DNA. Deamination of cytosine (C) to uracil (U) residues occurs primarily at single-stranded DNA overhangs and leaves characteristic patterns of C to T substitutions in sequences obtained from ancient DNA molecules, because uracils are read as thymines (T) by DNA polymerases. When we measured the number of fragments that contain C to T substitutions relative to the mtDNA consensus sequence, we found that this value was 0.4–0.7%. When we only take fragments with C to T substitutions in the first or last position, the frequency of C to T substitutions at the other end of the fragment is 2.1–3.7%. In conclusion, this mandible shows no evidence suggesting the presence of ancient human DNA.

Ancient protein analysis. *Protein extraction.* Separate bone and dentine samples (Supplementary Fig. 1) were drilled at the Key Laboratory of Western China's Environmental Systems (Ministry of Education), Lanzhou University. Dentine and bone samples were treated using established proteome extraction protocols[21,54]. This resulted in an ammonium bicarbonate fraction and acid-demineralization fraction for each sample. An extraction blank followed the exact same extraction procedure to estimate protein contamination during protein extraction and analysis.

MALDI–TOF-MS. Matrix-assisted laser desorption/ionization–time-of-flight mass spectrometry (MALDI–TOF-MS) analysis was carried out according to protocols established elsewhere[21,54,55]. Positive MALDI spectra were obtained for the dentine fractions in the low molecular range (less than 2,500 m/z) only. Ammonium-bicarbonate and acid-demineralization extractions of the bone sample returned negative MALDI spectra in all cases. Only the acid-demineralization and ammonium bicarbonate fractions of the dentine sample were therefore analysed using shotgun proteomics.

LC–MS/MS. Liquid chromatography tandem mass spectrometry (LC–MS/MS) was conducted on an Orbitrap Fusion Lumos in tandem with an Ultimate 3000 RSLCnano UPLC (both Thermo Fisher Scientific). Chromatographic separation of peptides was achieved on an EASY Spray PepMAP UHPLC column (50 cm × 75 μm, 2 μm particle size) after trapping on a PepMAP u-pre-column (0.5 cm × 300 μm). Peptides were eluted with a linear gradient of 5–35% acetonitrile in 5% DMSO/0.1% formic acid, followed by column washing and equilibration steps. Each sample was followed by a blank injection to evaluate sample carry-over. MS1 spectra were acquired between 400 and 1,500 Th in the orbitrap detector with a resolution of 120,000 and an automatic gain control (AGC) target of 400,000. Selected precursors were excluded for 7 s before repeated analysis in the Orbitrap at a resolution of 15,000 and after higher-energy collisional dissociation fragmentation (28% normalized collision energy). Precursors were isolated in the quadrupole with an isolation window of 1.2 Th. The instrument used a top speed duty cycle (3 s) with a maximum injection time of 40 ms and automatic gain control target of 40,000.

LC–MS/MS analysis of the ammonium bicarbonate and acid-demineralization fractions was conducted on three separate occasions. Ammonium bicarbonate and acid-demineralization extracts were analysed separately as well, resulting in six ancient protein files. In addition to injection blanks, extraction blanks were analysed twice, preceding and followed by injection blanks. All of the blank samples remained empty of appreciable amounts of proteins, and only included common laboratory contaminants.

Data analysis. Mass spectrometry files (.raw) from ancient samples, extraction blanks and injection blanks were converted to .mgf files using ProteoWizard[56]. Files resulting from the same extraction were searched together in PEAKS v.7[57]. Deamidation (NQ), oxidation (M), hydroxylation (P), pyro-glu (EQ) and phosphorylation (HCDRSTY) of the indicated amino acids were selected as variable modifications. MS1 tolerance was set at 10 p.p.m. and MS2 tolerance at 0.07 Da. Peptides were only accepted with a false discovery rate of $\leq$1.0%, with a minimum of 2 unique peptides for each protein with a total score of $-10 \times \log_{10}(P) \geq 20$. The first search was run against the entire human proteome database with the addition of Neanderthal- and Denisovan-specific protein sequences for a selected set of common bone and dentine proteins. The acceptance of amino acid substitutions in comparison to the provided sequence database followed the previously published guidelines[10]. Example MS/MS spectra of phylogenetically informative sequences can be found in Supplementary Fig. 4. The database was supplemented with a list of proteins commonly suspected to represent contaminant proteins[58].

For MALDI–TOF-MS spectra, glutamine deamidation was quantified for P1105, the collagen peptide appearing at an m/z of 1105.6, as this is a slow-deamidating peptide frequently observed in collagen MALDI–TOF-MS spectra[59]. For LC–MS/MS datasets, the extent of glutamine and asparagine deamidation was calculated as the ratio of spectra that contained deamidated glutamine and/or asparagine positions to the total number of spectra that contained glutamine and/or asparagine positions for each protein identified individually[21]. Contamination-filtering left eight collagens as likely endogenous to the Xiahe dentine proteome (Extended Data Table 2).

In addition to deamidation, we used a similar approach based on counts of peptide–spectrum matches (PSMs) to get an insight into peptide cleavage sites (both N and C termini of each peptide). One would expect modern proteins to have few or no non-enzymatic cleavages, whereas proteins preserved for extended periods of time might have undergone hydrolysis. Such hydrolysis would appear as non-proteotypic cleavage in resulting fragmention spectra. We normalized the obtained PSM counts in comparison to a random cleavage model for each investigated protein. To this end, human reference sequences for 12 selected proteins present in the Xiahe protein extracts were randomly cleaved, N- and C-terminal amino acid cleavage windows (positions P1 and P1′) were obtained for all the PSMs matching a particular protein and the observed percentage was divided by the theoretical percentage for random cleavage for each protein. We observed a large amount of semi-tryptic or non-tryptic PSMs in the endogenous collagens whereas such PSMs were almost absent in contaminants (Extended Data Fig. 5). In addition, for the endogenous collagens, we observed a far greater enrichment of cleavages after arginines (R, mainly R|G cleavages) compared to lysines (K, mainly K|G cleavages). The source of this difference is unclear, although a similar difference does not seem to be present for the contamination proteins. Therefore, its origin may lie in diagenetic modifications of lysines—for example, lysine methylation—that would make modified lysines inaccessible to trypsin cleavage.

Phylogenetic analysis. Of those proteins endogenous to the Xiahe dentine sample, six proteins were used for subsequent phylogenetic analysis (COL1α1, COL1α2, COL2α1, COL3α1, COL5α1 and COL5α2). Proteins COL9α1 and COL11α2 were excluded, because these proteins had a low number of matching peptides in both the acid-demineralization and ammonium bicarbonate extractions (Extended Data Table 2). COL10α1 protein sequences were added to the used protein sequence alignment for all included individuals, as we previously demonstrated that this protein is highly informative within archaic hominins[21]. Protein sequences were aligned with the homologous sequences from all genera of great ape and translated protein sequences from ancient hominin genomes (Neanderthals[60] and a Denisovan[61]); a macaque (*Macaca mulatta*) and a gibbon (*Nomascus leucogenys*) were used as outgroups. See Supplementary Table 5 for accession numbers.

Phylogenetic trees were built on the CIPRES Science Gateway[62] using MrBayes Bayesian phylogenetic analysis and RAxML maximum-likelihood methods. The protein sequence alignment was partitioned by gene for both analyses, allowing for variable substitution rates between genes using the Dayhoff substitution model. MrBayes was run for 5 million generations, with sampling every 500 generations and 10% was discarded as burn-in, while RAxML was run for 1,000 bootstrap iterations.

Reporting summary. Further information on research design is available in the Nature Research Reporting Summary linked to this paper.

Data availability

All the proteomic mass spectrometry data have been deposited in the ProteomeXchange Consortium repository (http://www.proteomexchange.org/) with the identifier PXD011377. Protein consensus sequences for the Xiahe hominin used for phylogenetic analysis are available in Supplementary Information 2. A surface scan model of the Xiahe mandible is publicly available at: https://www.eva.mpg.de/evolution/downloads/registration-form-xiahe.html.

Code availability

All R code used to generate protein deamidation and peptide cleavage patterns are available upon request from F.W (frido.welker@palaeo.eu).

32. Madsen, D. B. et al. Early foraging settlement of the Tibetan Plateau highlands. *Archaeol. Res. Asia* **11**, 15–26 (2017).
33. Brantingham, J. P. et al. in *Developments in Quaternary Sciences* **9**, 129–150 (Elsevier, Amsterdam, 2007).
34. Shen, C.-C. et al. Variation of initial $^{230}Th/^{232}Th$ and limits of high precision U–Th dating of shallow-water corals. *Geochim. Cosmochim. Acta* **72**, 4201–4223 (2008).
35. Shen, C.-C. et al. High-precision and high-resolution carbonate ^{230}Th dating by MC-ICP-MS with SEM protocols. *Geochim. Cosmochim. Acta* **99**, 71–86 (2012).
36. Wiley, D. F. et al. Evolutionary morphing. *Proc. IEEE Visualization* 431–438 (2005).
37. Gunz, P. & Mitteroecker, P. Semilandmarks: a method for quantifying curves and surfaces. Hystrix It. *J. Mamm.* **24**, 103–109 (2013).
38. Mitteroecker, P. & Bookstein, F. Linear discrimination, ordination, and the visualization of selection gradients in modern morphometrics. *Evol. Biol.* **38**, 100–114 (2011).
39. Copes, L. *Comparative and Experimental Investigations of Cranial Robusticity in Mid-Pleistocene Hominins* PhD thesis, Arizona State Univ. (2012).
40. Mardia, K. V., Bookstein, F. L. & Moreton, I. J. Statistical assessment of bilateral symmetry of shapes. *Biometrika* **92**, 249–250 (2005).
41. Rohlf, F. J. & Slice, D. Extensions of the Procrustes method for the optimal superimposition of landmarks. *Syst. Biol.* **39**, 40–59 (1990).
42. Bookstein, F. L. *Morphometric Tools for Landmark Data: Geometry and Biology* (Cambridge Univ. Press, 1997).
43. Stelzer, S., Gunz, P., Neubauer, S. & Spoor, F. Using the covariation of extant hominoid upper and lower jaws to predict dental arcades of extinct hominins. *J. Hum. Evol.* **114**, 154–175 (2018).
44. Stelzer, S., Neubauer, S., Hublin, J.-J., Spoor, F. & Gunz, P. Morphological trends in arcade shape and size in Middle Pleistocene *Homo*. *Am. J. Phys. Anthropol.* **168**, 70–91 (2019).
45. Spoor, F. et al. Reconstructed *Homo habilis* type OH 7 suggests deep-rooted species diversity in early *Homo*. *Nature* **519**, 83–86 (2015).
46. Mathematica v.5.1 (Wolfram Research, 2004).
47. Turner, C. G. II, Nichol, C. R. & Scott, G. R. in *Advances in Dental Anthropology* (eds Kelley, M. A. & Larsen, C. S.) 13–31 (Wiley-Liss, New York, 1991).
48. Skinner, M. M., Gunz, P., Wood, B. A. & Hublin, J.-J. Enamel–dentine junction (EDJ) morphology distinguishes the lower molars of *Australopithecus africanus* and *Paranthropus robustus*. *J. Hum. Evol.* **55**, 979–988 (2008).
49. Skinner, M. M., Gunz, P., Wood, B. A., Boesch, C. & Hublin, J.-J. Discrimination of extant *Pan* species and subspecies using the enamel–dentine junction morphology of lower molars. *Am. J. Phys. Anthropol.* **140**, 234–243 (2009).
50. Dabney, J. et al. Complete mitochondrial genome sequence of a Middle Pleistocene cave bear reconstructed from ultrashort DNA fragments. *Proc. Natl Acad. Sci. USA* **110**, 15758–15763 (2013).
51. Gansauge, M.-T. & Meyer, M. Single-stranded DNA library preparation for the sequencing of ancient or damaged DNA. *Nat. Protoc.* **8**, 737–748 (2013).
52. Fu, Q. et al. DNA analysis of an early modern human from Tianyuan Cave, China. *Proc. Natl Acad. Sci. USA* **110**, 2223–2227 (2013).
53. Li, H. & Durbin, R. Fast and accurate short read alignment with Burrows–Wheeler transform. *Bioinformatics* **25**, 1754–1760 (2009).
54. Welker, F., Soressi, M., Rendu, W., Hublin, J.-J. & Collins, M. J. Using ZooMS to identify fragmentary bone from the late Middle/Early Upper Palaeolithic sequence of Les Cottés, France. *J. Archaeol. Sci.* **54**, 279–286 (2015).
55. Welker, F. et al. Variations in glutamine deamidation for a Châtelperronian bone assemblage as measured by peptide mass fingerprinting of collagen. *Sci. Technol. Archaeol. Res.* **3**, 15–27 (2017).
56. Chambers, M. C. et al. A cross-platform toolkit for mass spectrometry and proteomics. *Nat. Biotechnol.* **30**, 918–920 (2012).
57. Zhang, J. et al. PEAKS DB: de novo sequencing assisted database search for sensitive and accurate peptide identification. *Mol. Cell. Proteomics* **11**, M111.010587 (2012).
58. Hendy, J. et al. A guide to ancient protein studies. *Nat. Ecol. Evol.* **2**, 791–799 (2018).
59. van Doorn, N. L., Wilson, J., Hollund, H., Soressi, M. & Collins, M. J. Site-specific deamidation of glutamine: a new marker of bone collagen deterioration. *Rapid Commun. Mass Spectrom.* **26**, 2319–2327 (2012).
60. Castellano, S. et al. Patterns of coding variation in the complete exomes of three Neandertals. *Proc. Natl Acad. Sci. USA* **111**, 6666–6671 (2014).
61. Meyer, M. et al. Nuclear DNA sequences from the Middle Pleistocene Sima de los Huesos hominins. *Nature* **531**, 504–507 (2016).
62. Miller, M. A., Pfeiffer, W. & Schwartz, T. Creating the CIPRES Science Gateway for inference of large phylogenetic trees. In Gateway *Computing Environments Workshop* 1–8 (2010).
63. Hiess, J., Condon, D. J., McLean, N. & Noble, S. R. $^{238}U/^{235}U$ Systematics in terrestrial uranium-bearing minerals. *Science* **335**, 1610–1614 (2012).
64. Cheng, H. et al. Improvements in ^{230}Th dating, ^{230}Th and ^{234}U half-life values, and U–Th isotopic measurements by multi-collector inductively coupled plasma mass spectrometry. *Earth Planet. Sci. Lett.* **371–372**, 82–91 (2013).
65. Jaffey, A. H., Flynn, K. F., Glendenin, L. E., Bentley, W. C. & Essling, A. M. Precision measurement of half-lives and specific activities of ^{235}U and ^{238}U. *Phys. Rev. C* **4**, 1889–1906 (1971).
66. Welker, F. et al. Middle Pleistocene protein sequences from the rhinoceros genus *Stephanorhinus* and the phylogeny of extant and extinct Middle/Late Pleistocene Rhinocerotidae. *PeerJ* **5**, e3033 (2017).

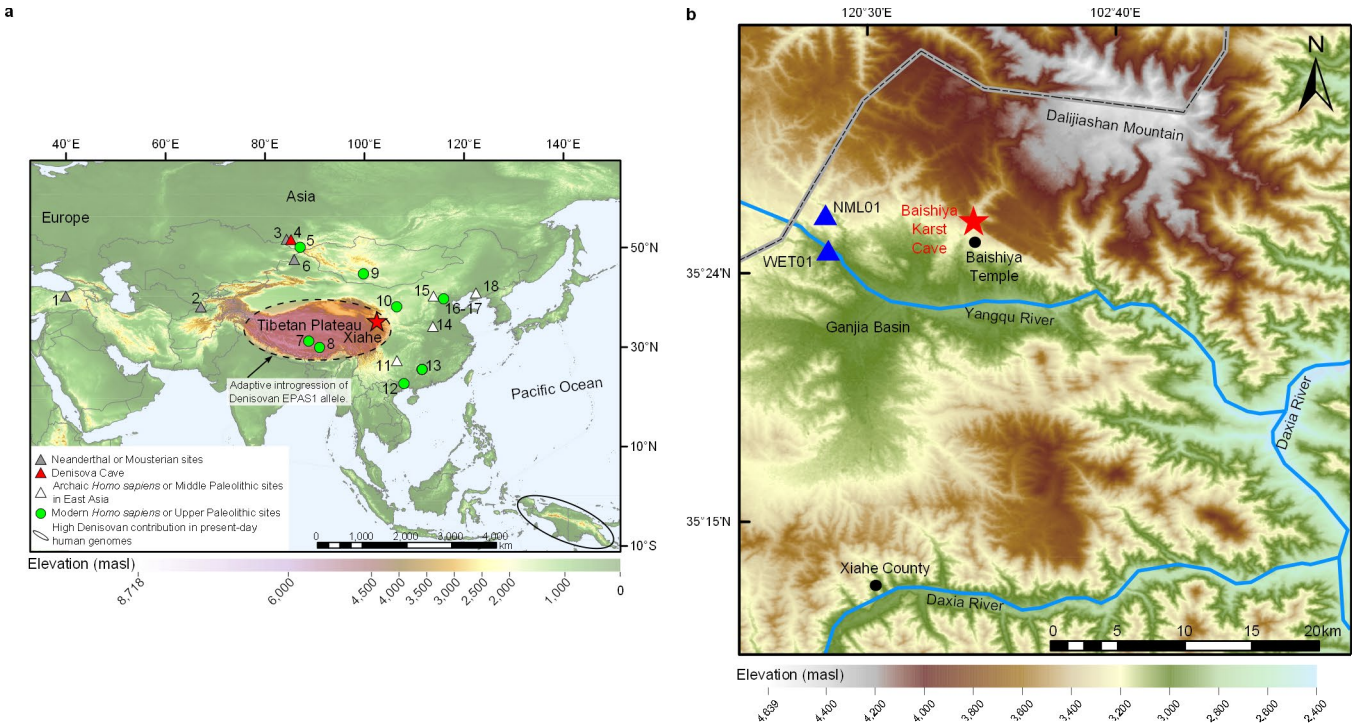

Extended Data Fig. 1 | Location of Baishiya Karst Cave. a, Location of Baishiya Karst Cave, archaic *Homo* sites, and selected Middle and Upper Palaeolithic sites in East and Central Asia. Numbers denoting the archaeological sites are: (1) Mezmaiskaya Cave; (2) Teshik-Tash Cave; (3) Okladnikov Cave; (4) Denisova Cave; (5) Kara-Bom; (6) Tongtian Cave; (7) Nyadem; (8) Quesang; (9) Chikhen Agui; (10) Shuidonggou; (11) Guanyin Cave, (12) Zhiren Cave; (13) Fuyan Cave; (14) Lingjing; (15) Xujiayao; (16) Tianyuan Cave; (17) Zhoukoudian Upper Cave; (18) Jinniushan. Denisovan ancestry is also detectable in other East and South Asian populations at low frequencies. **b**, Ganjia Basin with the Baishiya Karst Cave (red star) and two Palaeolithic sites (NML01, Nimalong01; WET01, Waerta01; blue triangles). Base maps generated by ArcGIS 10.3 using DEM data provided by https://earthexplorer.usgs.gov/.

Extended Data Fig. 2 | The Xiahe mandible with adhering carbonate crust. a–**f**, Lateral (**a**), buccal (**b**), occlusal (**c**), inferior (**d**), anterior (**e**) and posterior (**f**) views. Sampling locations for ancient proteins and ancient DNA can be seen on the M_2 and ascending ramus, and sampling location for U–Th dating on the inferior surface.

Extended Data Fig. 3 | Surface model of the Xiahe mandible after digital removal of the adhering carbonate crust. a–f, Lateral (**a**), buccal (**b**), occlusal (**c**), inferior (**d**), anterior (**e**) and posterior (**f**) views.

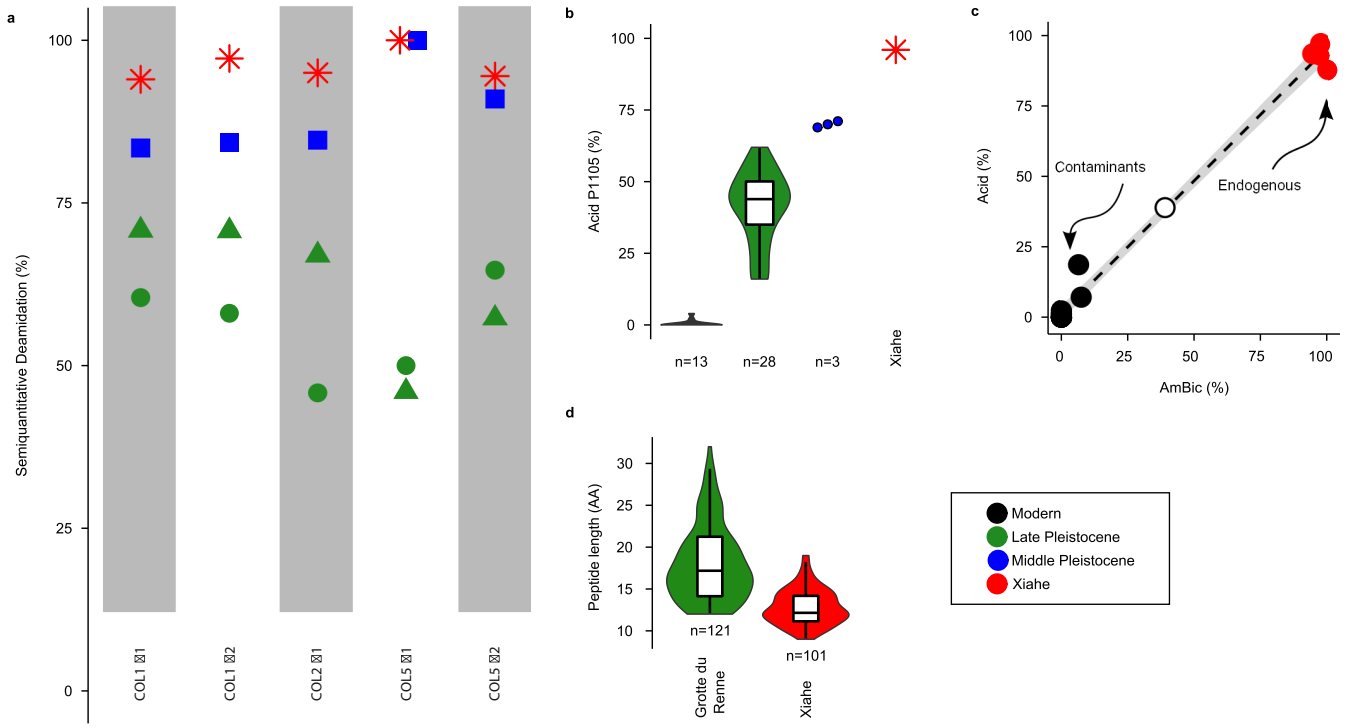

Extended Data Fig. 4 | Preservation of the Xiahe dentine proteome. **a**, Deamidation of five Xiahe proteins also identified in several proteomes from Middle and Late Pleistocene hominin fossils. **b**, Glutamine deamidation of peptide P1105 observed in the ZooMS analysis of the Xiahe dentine sample compared to reference data. *n* = number of specimens included. **c**, Correlation between deamidation observed in LC–MS/MS experiments for ammonium bicarbonate (AmBic) and acid-demineralization (Acid) extracts ($R^2 = 0.99$). **d**, Length distribution of non-tryptic peptides in a Late Pleistocene Neanderthal and the Xiahe dentine proteome. AA, amino acids. Violins stretch from the minimum to the maximum value; box plots indicate the median (middle line), 25% and 75% (boxes) and stretch to 1.5× the interquartile range (whiskers). *n* = number of unique spectra included. Deamidation is based on quantitative MALDI–TOF-MS analysis (**b**) or semiquantitative LC–MS/MS spectral counting methods (**a**, **c**). '0%' indicates an absence of deamidation and '100%' indicates complete deamidation of asparagine and glutamine. **a**, **d**, Combined data for all six LC–MS/MS runs conducted on the Xiahe protein extracts. **c**, Combined data from the three replicates per extraction method. Samples are colour-coded according to geological age. Data were obtained from previous studies[21,54,55,66].

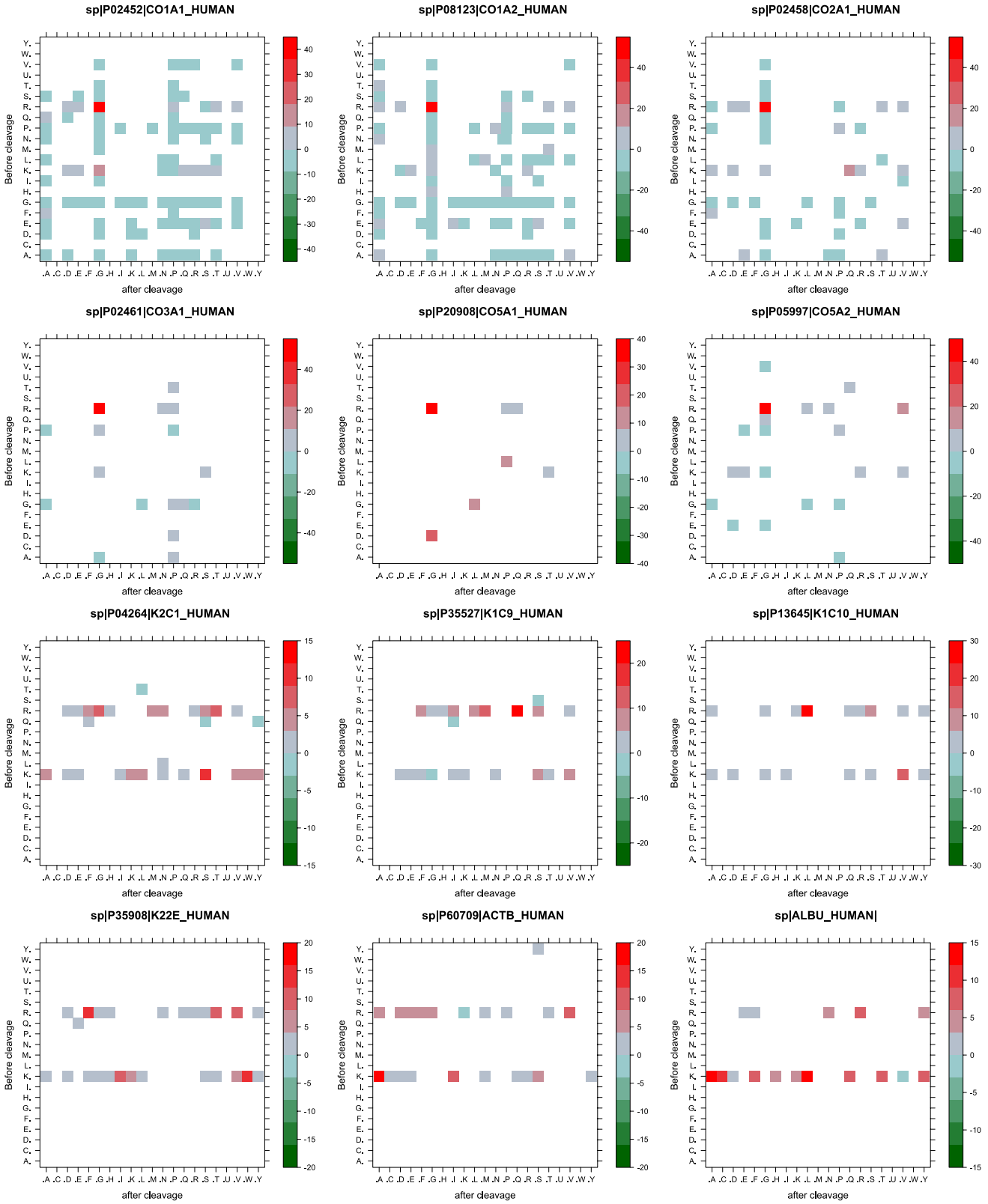

Extended Data Fig. 5 | Normalized frequencies of peptide cleavage patterns of selected proteins. Spectral counts are based on the total number of ammonium bicarbonate and acid-demineralization PSMs (six runs) and include both N and C termini of each aligned PSM. Red colours indicate more PSMs than expected and green colours fewer PSMs than expected, compared to a random cleavage model for each protein separately. Note differences in colour scale. The title of each plot refers to the UniProt accession code for the relevant protein.

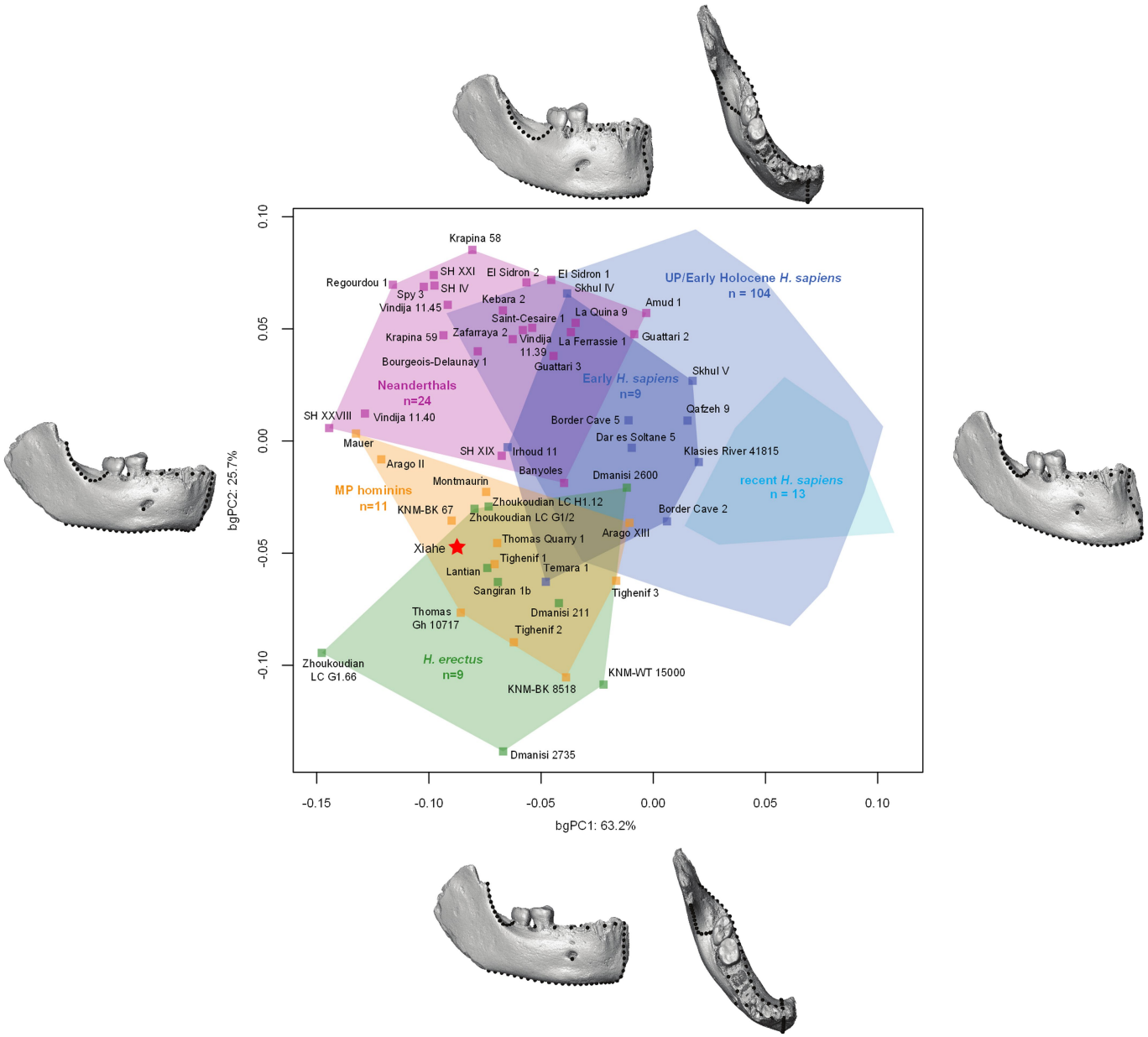

Extended Data Fig. 6 | Geometric morphometrics of the mandible. bgPCA of mandibular shape. Although some overlap exists, all groups show a distinct mandibular shape. Xiahe plots at the edge of the *H. erectus* distribution and within the range of Middle Pleistocene *Homo*. Surface models illustrate mandibular shape changes along bgPC1 (lateral view) and bgPC2 (lateral and superior view). Recent *H. sapiens* are shown in cyan, Upper Palaeolithic and Holocene *H. sapiens* in light blue, early *H. sapiens* in dark blue, Neanderthals in pink, *H. erectus* in green and other Middle Pleistocene fossil hominins in orange. SH, Sima de los Huesos. *n* = number of unique individuals contained in each hull. Further specimen names can be found in Supplementary Table 6.

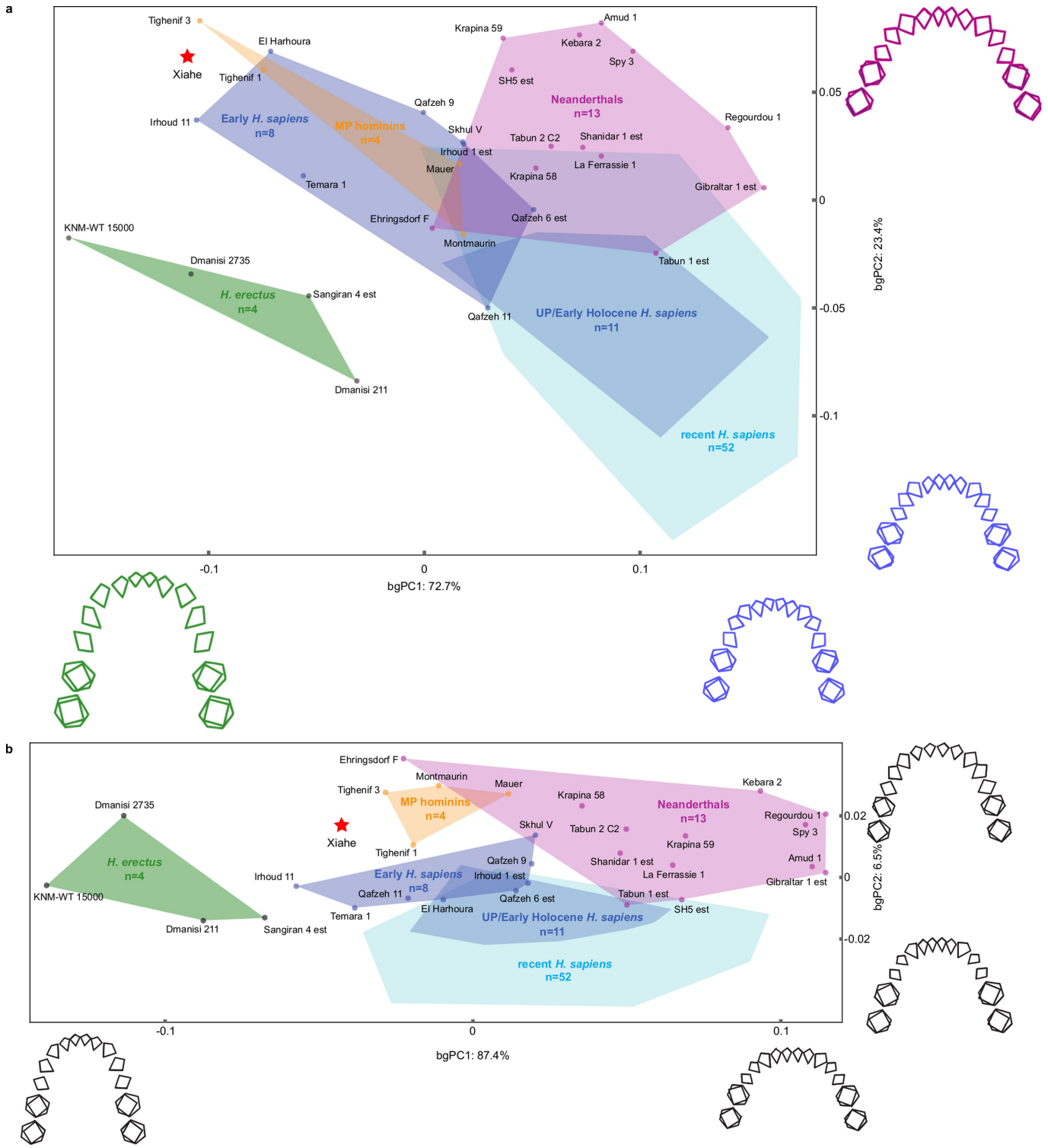

Extended Data Fig. 7 | Geometric morphometrics of the dental arcade. **a**, bgPCA in form space. **b**, bgPCA in shape space. The wireframes illustrate form changes along bgPC1 and bgPC2. Colours are as in Extended Data Fig. 6. The wireframes show the form and shape changes along bgPC1 and bgPC2, respectively. Estimated wireframes used in the bgPCA are indicated by 'est'. SH, Sima de los Huesos; D, Dmanisi. Further specimen names can be found in Supplementary Table 6. *n* = number of unique individuals contained in each hull.

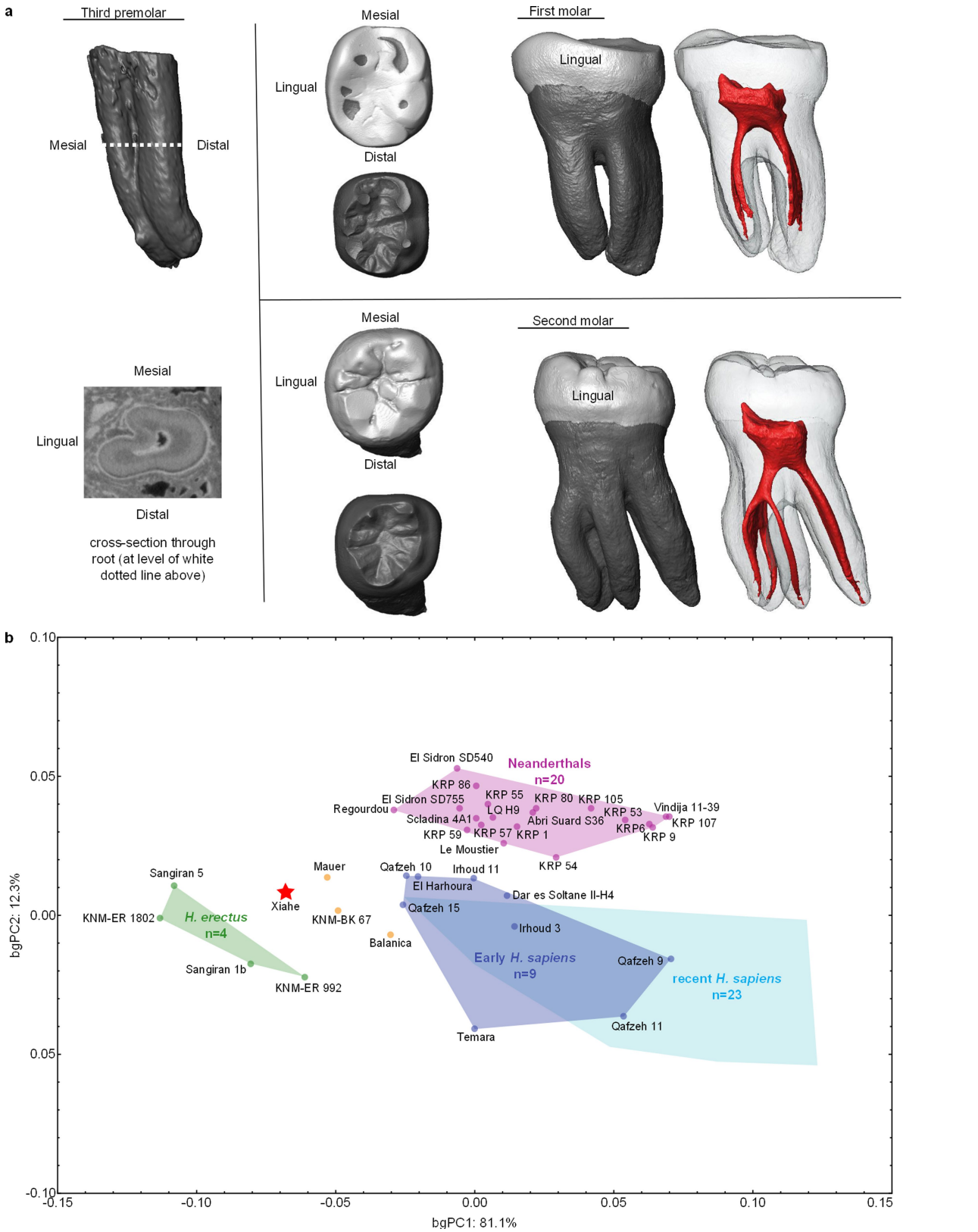

Extended Data Fig. 8 | Root morphology and EDJ shape. a, The roots of the M_1 are typical of lower molars with a mesial and distal plate-like root. There are mesial and distal plate-like roots on the M_2; however, there is an additional accessory lingual root that splits off distally from the mesial root about 2/3 from the cervix. The P_3 root is a Tomes' form with a distinct lingual groove. **b**, A bgPCA of the EDJ ridge and cervix shape reveals a clear separation between early *Homo* and *H. erectus* on one side and Neanderthals and *H. sapiens* on the other side, with Middle Pleistocene hominins in between. Colours are as in Extended Data Fig. 6 for relevant groups. KRP, Krapina; LQ, La Quina. *n* = number of unique individuals contained in each hull. Note that the taxonomic status of Sangiran 5 is currently uncertain. Further specimen names can be found in Supplementary Table 6.

Extended Data Table 1 | U–Th ages of the crust attached on Xiahe mandible

Subsample	Weight	^{238}U	^{232}Th	$\delta^{234}U$	$[^{230}Th/^{238}U]$	$^{230}Th/^{232}Th$	Age (ka)	Age (ka BP)	$\delta^{234}U_{initial}$
ID	g	10^{-6} g/g [a]	10^{-6}g/g	measured [a]	activity [c]	atomic (x 10^{-6})	uncorrected	corrected [c,d]	corrected [b]
XH-SD-U1	0.2198	1348.5 ± 2.1	316.0 ± 4.2	431.1 ± 2.7	1.195 ± 0.020	84.1 ± 1.8	168.3 ± 6.1	164.5 ± 6.2	686 ± 13
XH-SD-U4	0.1837	1523.2 ± 2.8	330 ± 12	388.5 ± 2.6	1.122 ± 0.052	85.4 ± 5.0	158 ± 15	155 ± 15	601 ± 28
XH-SD-U6	0.1962	1464.1 ± 2.5	477 ± 16	411.2 ± 2.7	1.177 ± 0.031	59.5 ± 2.5	169 ± 10	163 ± 10	652 ± 19

[a] $[^{238}U] = [^{235}U] \times 137.818$ (±0.65‰)[63]; $\delta^{234}U = ([^{234}U/^{238}U]_{activity} - 1) \times 1{,}000$.
[b] Corrected $\delta^{234}U_{initial}$ values were calculated based on ^{230}Th age (T), that is, $\delta^{234}U_{initial} = \delta^{234}U_{measured} \times e^{\lambda 234 T}$, and T is the corrected age.
[c] $[^{230}Th/^{238}U]_{activity} = 1 - e^{-\lambda 230 T} + (\delta^{234}U_{measured}/1{,}000)[\lambda_{230}/(\lambda_{230} - \lambda_{234})](1 - e^{-(\lambda 230 - \lambda 234)T})$, where T is the age. Decay constants (λ) are 9.1705×10^{-6} yr^{-1} for ^{230}Th, 2.8221×10^{-6} yr^{-1} for ^{234}U, as calculated in a previous study[64] and 1.55125×10^{-10} yr^{-1} for ^{238}U, as calculated in a previous study[65].
[d] Age corrections, relative to AD 1950, were calculated using an estimated initial atomic $^{230}Th/^{232}Th$ ratio of 4 (± 2) $\times 10^{-6}$.
U–Th isotopic compositions, activity and ^{230}Th age uncertainties are 2σ.

Extended Data Table 2 | Endogenous protein coverage statistics

	AmBic		Acid		Combined		
Protein	Peptides	Unique	Peptides	Unique	Coverage (%)	N_Deam (%)	Q_Deam (%)
COL1α1	539	499	375	349	61.1 (88.2)	99.2 (733)	91.8 (2018)
COL1α2	346	338	243	236	54.8 (73.8)	98.0 (1368)	92.7 (280)
COL2α1	78	38	61	38	25.2	89.7 (29)	95.6 (247)
COL3α1	34	28	7	4	7.0	0 (8)	83.3 (18)
COL5α1	7	5	6	4	2.6	-	100 (3)
COL5α2	28	22	27	24	11.1	72.73 (11)	96.9 (96)
COL9α1	3	3	-	-	-	-	100 (9)
COL11α2	7	4	5	4	-	-	87.5 (8)

Triple-helical coverage is indicated in parentheses for COL1α1 and COL1α2 as the non-triple-helical regions of COL1α1 and COL1α2 are not present in the mature COL1 protein, and therefore not observed in most proteome studies. N_Deam: asparagine deamidation. Q_Deam: glutamine deamidation. Number of spectra (PSMs) covering asparagine and glutamine are indicated in parentheses for both deamidation columns.